Single-Cell Photoacoustic Microrheology

Fen Yang, Zhongjiang Chen, and Da Xing

***Abstract*— Rheological properties, such as elasticity and viscosity, are fundamental biomechanical parameters that are related to the function and pathological status of cells and tissues. In this paper, an innovative photoacoustic microrheology (PAMR), which utilized the time and phase characteristics of photoacoustic (PA) response, was proposed to extract elastic modulus and viscosity. The feasibility and accuracy of the method were validated by tissue-mimicking agar-gelatin phantoms with various viscoelasticity values. PAMR realized single cell elasticity and viscosity mappings on the adipocyte and myocyte with micrometer scale. In clinical samples, normal blood cells and iron deficiency anemia cells were successfully distinguished due to their various rheological properties. This method expands the scope of conventional PA imaging and opens new possibilities for developing microrheological technology, prefiguring great clinical potential for interrogating mechanocellular properties.**

***Index Terms*— Photoacoustic, viscoelasticity imaging, cell, biomechanical model.**

I. Introduction

MICRORHEOLOGY tools for studying cellular rheological properties have opened up a new way of thinking about how cells function [1]–[3]. Rheological properties such as elasticity and viscosity correlate with physiological function and pathological state of cells, and have been recognized as an indication of many diseases [4], [5]. Several constituents, including cytoskeleton, cell membrane, and cell nucleus, contribute to the cellular rheological properties. The cytoskeleton can be assumed as a relatively rigid framework [6]. The cell membrane plays a particularly significant role in maintaining cellular viscoelasticity, since viscoelasticity influences the activity of membrane-bound proteins [7], [8]. For example, the cell membrane can harden or soften to modulate passage of biomolecules [8]. Nuclear stiffness is strongly correlated with gene signaling and gene transcription [9], and has also been shown to regulate cell phenotype during the stem cell differentiation [10].

Currently, many techniques have been established to evaluate viscoelastic properties of tissues and cells. The ultrasound technique [11]–[13] and optical elastography [14], [15] estimate elasticity or viscosity by measuring the shear wave propagation speed of tissues. However, the measurement of the propagation speed naturally diminishes the accuracy of elasticity and viscosity estimations, especially for heterogeneous biological tissue. The tweezing techniques, including optical [16], acoustic [17] and magnetic tweezers [18], micropipette aspiration [19], and deformability cytometry [20], measure cellular deformation by applying shear stresses or pressure gradients in suspension, which renders these techniques both invasive and subject to strong non-linear effects [21]. Atomic force microscopy measures elasticity from the static cell deformation under an external force [22]. The mechanical loading, however, potentially induces a certain damage to the sample. Moreover, the operational manner with preload does not facilitate the technical implementation, thus greatly limiting the applications in the biological science. Recently, Brillouin spectroscopy has been presented to non-invasively assess elasticity by measuring Brillouin frequency shift of acoustic phonons [23]. While this is a powerful method to interrogate cellular or even intracellular biomechanical properties, extending the Brillouin technique from point sampling spectroscopy to imaging modality has been a challenge, mainly because rapid spectrum acquisition is required, which renders the approach low throughput [23], [24].

Photoacoustic (PA) imaging, as a rapidly developing non-invasive technology, has been widely used in biomedical imaging, image-guided drug delivery, and preclinical diagnostics [25]–[27]. There have been several PA studies on characterization of the elastic properties. In one study, PA elastography was developed based on measuring the static deformation of tissue under an external compressive force [28]. However, friction between the mechanical loading plate and the tissue surface restricted the lateral expansion of the tissue at the boundary during loading, resulting in an overestimation of the elastic modulus [24]. In addition, as mentioned previously, the mode with mechanical compression was undesirable or unserviceable for many clinical settings. The second study showed the attribution of the elastic property to PA signals,

Manuscript received November 22, 2019; accepted November 28, 2019. Date of publication December 6, 2019; date of current version June 1, 2020. This work was supported in part by the National Natural Science Foundation of China under Grant 61627827, Grant 81630046, Grant 91539127, and Grant 61705068, in part by the National High Technology Research and Development Program of China under Grant 2015AA020901, in part by the Science and Technology Planning Project of Guangdong Province, China, under Grant 2015B020233016 and Grant 2014B020215003, and in part by the Ph.D. Start-Up Fund of Natural Science Foundation of Guangdong Province under Grant 2017A030310363. *(Corresponding author: Da Xing.)*

The authors are with the MOE Key Laboratory of Laser Life Science and Institute of Laser Life Science, South China Normal University, Guangzhou 510631, China, and also with the College of Biophotonics, South China Normal University, Guangzhou 510631, China (e-mail: yangfen@scnu.edu.cn; chenchj@scnu.edu.cn; xingda@scnu.edu.cn).

This article has supplementary downloadable material available at http://ieeexplore.ieee.org, provided by the authors.

Color versions of one or more of the figures in this article are available online at http://ieeexplore.ieee.org.

Digital Object Identifier 10.1109/TMI.2019.2958112

but did not extract the elastic modulus because of the inability to distinguish the contrast in PA intensity from elastic and optical absorption coefficients [29]. In another study, multi-spectral PA elasticity tomography was reported to assess the elastic modulus, based on the known spectral characteristics of specific chromophores [30]. However, the absorption spectra were not usually known *a priori* due to the complexity and heterogeneity of biological samples. Moreover, the measurement was performed with multi-wavelength excitation, which is time-consuming.

We have previously developed a PA viscoelasticity imaging technique that extracts the viscosity-elasticity ratio parameter with the PA phase delay [31]–[33]. The technique makes it possible to obtain a non-invasive mapping of viscoelastic properties without extrinsic mechanical loading and with only one excitation, and has been successfully utilized in breast cancer detection [32] and arterial plaque assessment [34], [35]. However, the contrast based on the viscosity-elasticity ratio instead of both the elasticity and viscosity limits the ability to distinguish cell types. And though the elasticity values and viscosity values of two types of cells differ respectively, the two types of cells can produce same viscosity-elasticity ratio. In this paper, we further explore the time characteristics of the PA response, and propose an innovative PA microrheology (PAMR) to simultaneously extract elastic modulus and viscosity. Quantitative mappings of both elasticity and viscosity would represent a more complete indication of rheological properties, thus potentially enhancing the ability to reliably distinguish tissue or cell types.

II. Materials and Methods

In this section, we propose a PAMR method based on the thermoelastic expansion and damping effect. In Sec. II-A, by establishing a biomechanical model, elasticity and viscosity can be determined by exploring the time and phase characteristics of PA response. In Sec. II-B, we numerically simulate the displacement with various rheological parameters. In Sec. II-C, we set up the PAMR system. In Sec. II-D, the preparation of the experimental phantom and cell samples are introduced. In Sec. III, appropriate examples are provided in order to show the feasibility of the PAMR method.

A. Theoretical Foundations

1) Estimation of Elastic Modulus: Based on the thermal expansion mechanism, irradiation of the absorbing region with a laser pulse will induce oscillation of the sample and then generate the PA pressure wave, as illustrated in Fig. 1(a). Considering a linear, isotropic, and viscoelastic medium, Navier's equation governs the displacement at each laser-excited point of the sample [36]

$$\rho\frac{\partial^2\mathbf{u}}{\partial t^2} = (\lambda+\mu)\nabla(\nabla\cdot\mathbf{u}) + \mu\nabla^2\mathbf{u} + (\varepsilon+\eta_0/3)\frac{\partial}{\partial t}\nabla(\nabla\cdot\mathbf{u}) + \eta_0\frac{\partial}{\partial t}\nabla^2\mathbf{u} + \mathbf{F}. \quad (1)$$

Here ρ is the mass density, $\mathbf{u}$ is the displacement vector, λ and μ are the Lame' constants, ε is the bulk viscosity, η_0 is the shear viscosity, and $\mathbf{F}$ is defined as the equivalent excitation force induced by laser. Using Helmholtz decomposition $\mathbf{u} = \mathbf{u_p} + \mathbf{u_s}$, where $\mathbf{u_p}$ and $\mathbf{u_s}$ are, respectively, curl-free ($\nabla\times\mathbf{u}_p = 0$) and divergence-free ($\nabla\cdot\mathbf{u}_s = 0$) vector fields, two elastic waves can be retrieved [14], [37] (see Supplementary Note 1 for details). The two types of waves, the longitudinal wave and the shear wave, propagate independently in medium. In terms of expansion-induced PA waves as the longitudinal wave, the wave equation of the longitudinal wave form is considered. The longitudinal wave is known as the irrotational wave, i.e.,$\nabla\times\mathbf{u}_p = 0$. Equation (1) then becomes

$$\rho\frac{\partial^2 u_p}{\partial t^2} - (\lambda+2\mu)\nabla^2 u_p - (\varepsilon+4/3\eta_0)\frac{\partial}{\partial t}\nabla^2 u_p = F_{\text{exc}}. \quad (2)$$

We record the term $(\lambda+2\mu)$ as apparent elastic modulus E and the term $(\varepsilon+4/3\eta_0)$ as the apparent viscosity η. The excitation force F_{exc} with a Gaussian laser beam is described as $F_{exc} = \alpha\Gamma P/c \cdot f(t) \cdot \exp\left[-\alpha z - (r/R)^2\right]$ [38], [39]. Physically, the force means the transient pressure that results from an increase in temperature induced by photons absorption of biomolecules, based on the photothermal effect [31], [40]. Here α is the optical absorption coefficient, Γ is the Grüneisen parameter that defines the conversion efficiency of the absorbed photon energy to PA waves, P is the initial laser power density along the beam axis, c is the speed of light in vacuum, $f(t)$ describes the time dependence of the laser pulse, r is the radial coordinate, and R is the waist radius of the Gaussian laser beam. Equation (2) can be transformed into

$$\frac{\partial^2 u_p}{\partial t^2} - \left(\frac{E}{\rho} + \frac{\eta}{\rho}\frac{\partial}{\partial t}\right)\nabla^2 u_p = \frac{\alpha\Gamma P}{\rho c} f(t)\exp(-\alpha z - \frac{r^2}{R^2}). \quad (3)$$

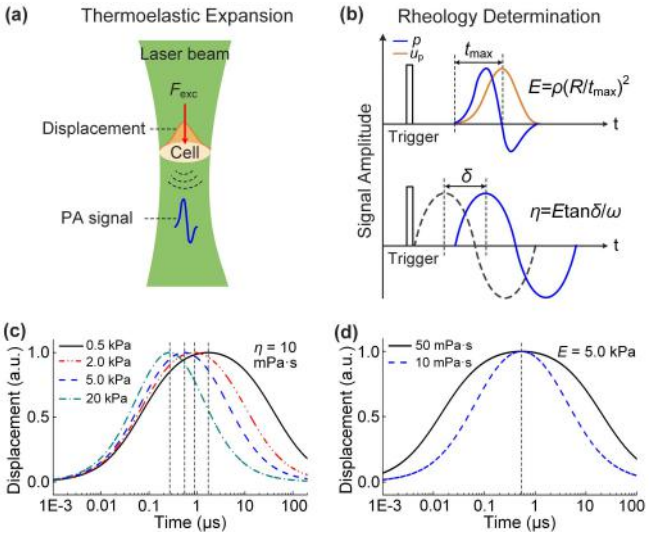

Fig. 1. Principle of PAMR and theoretical prediction of viscoelastic medium responses. (a) Laser-induced displacement and PA signals based on the thermoelastic expansion. (b) Extractions of the apparent elastic modulus E and apparent viscosity η by measuring the rise time t_{max} and phase delay δ of the PA response. (c) Simulated displacement for viscoelastic medium with various elastic moduli and a constant viscosity. (d) Simulated displacement for viscoelastic medium with various viscosities and a constant elastic modulus.

By using the Hankel transformation method, the displacement can be analytically solved at the focal spot as [41]

$$u_p = \frac{\sqrt{\pi}\alpha\Gamma RP\tau}{2c\sqrt{\rho E}} \frac{\left(\frac{\sqrt{E/\rho}}{R}\right)t}{1+\frac{2\eta}{\rho R^2}t+\left(\frac{\sqrt{E/\rho}}{R}\right)^2 t^2}. \tag{4}$$

Here, τ is the laser pulse width. Equation (4) indicates that the rise time $t_{\max}$ required for the displacement to reach maximum $u_{\max}$ at the focal point is related to elasticity of medium. The displacement increases initially after excitation, and reaches its peak at $t_{\max} = R/\sqrt{E/\rho}$, as illustrated in the top panel of Fig. 1(b). Thus, apparent elastic modulus E can be estimated by

$$E = \rho(R/t_{\max})^2 . \tag{5}$$

The PA wave originates from the expansion-induced displacement, as described by the relationship [42]

$$\nabla p = -\rho\frac{\partial^2 u_p}{\partial t^2} . \tag{6}$$

Where p is the PA pressure. Equation (6) is usually transformed into $u_p = -1/(\rho c_L)\int p dt$, where c_L is the sound velocity. The sample expansion corresponds to the compression wave, i.e., the positive part of the PA wave, and collapse corresponds to the rarefaction wave, i.e., the negative part of the PA wave, as shown in the top panel of Fig. 1(b). Thus, exploring the rise time of the PA-obtained displacement can reflect the elastic modulus.

The acquisition procedures about the rise time of the displacement by PA technique are summarized as follows: Firstly, the resultant displacement is obtained through the time integration of the time-domain PA signal. Secondly, the time t_2 at peak displacement is recorded, and the time zero t_1 is set, where the displacement approximately equals to the average noise amplitude. Then, the rise time $t_{\max}$ is obtained by $t_{\max} = (t_2\text{-}t_1)$.

2) Viscosity Estimation: In general, viscoelastic medium exhibits complex rheological behavior, showing classic elastic and viscous characteristics with time-dependent mechanical responses [43]. While subject to a stimulus, a viscoelastic medium does not instantaneously respond but gradually deforms as governed by its characteristic relaxation creep [44]. It means that the deformation responds to the external stimulus with a characteristic phase lag. In the case of the laser-induced PA wave, PA deformation responds to laser stimulus with a phase delay (i.e., phase lag), as shown in the bottom panel of Fig. 1(b). Based on the rheological Kelvin–Voigt (KV) model, the stress-strain (i.e., response-stimulus) constitutive equation can be expressed as [31]

$$\sigma(t) = E\varepsilon(t) + \eta\dot{\varepsilon}(t). \tag{7}$$

Where σ is the stress, and ε is the strain. By taking the Fourier transform of both sides of (7), and assuming that the stress and strain are cyclic (i.e., ε, $\sigma \sim e^{i\omega t}$), the KV model can be expressed as in the frequency domain $\sigma(\omega) = E\varepsilon(\omega) + i\omega\eta\varepsilon(\omega)$, where ω is the modulation frequency. The phase delay δ of the strain response (i.e., PA signal) to the stress (i.e., laser stimulus) is given by $\tan\delta = \eta\omega/E$. Here, an apparent viscosity η can be calculated with

$$\eta = E\tan\delta/\omega . \tag{8}$$

Therefore, according to (5) and (8), the apparent elastic modulus and apparent viscosity can be simultaneously extracted by the PA rise time and phase delay measurements.

B. Displacement Simulations

To understand the effects of elastic modulus and viscosity on the response, we numerically simulate the laser-induced displacement according to (4). In the simulation, the density and waist radius are assumed to be $\rho = 1000$ kg/m^3 and $R = 1.2$ μm, respectively. Fig. 1(c) provides temporal profiles of displacement with various elastic moduli E varying from 0.5 to 20 kPa and with a constant viscosity of $\eta = 0.01$ Pa·s. The result shows that the rise time of displacement decreases with the increase in the elastic modulus. Specifically, when the elastic modulus increases from 0.5 to 20 kPa, the rise time decreases $\sqrt{40}$ times (from 1.697 to 0.268 μs). Fig. 1(d) simulates the displacement profile for different viscosities of $\eta = 0.01$ Pa·s and $\eta = 0.05$ Pa·s and a constant elastic modulus $E = 5$ kPa. The results exhibit that, even though the profile of the displacement is affected by both the elastic modulus and viscosity, the rise time depends mainly on the elastic modulus, and viscosity has no effect on the rise time. The thermoelastic expansion effect essentially explains the elastic modulus as a determinant of the rate of displacement increase. Viscosity, as a loss modulus, determines the rate of the displacement decrease [41], [45].

C. Experimental Setup

The experimental setup of the PAMR is shown in Fig. 2. A laser operating at 532 nm (DTL-314QT, pulsed Q-switched Laser, Russia) with a 10 kHz repetition frequency and 10 ns pulse width served as the excitation source. The laser beams were expanded and collimated through a spatial filtering system, and then were scanned with a two-dimensional galvanometer scanner (GM, 6231H; Cambridge Technology, Inc., U.S.). After passing through a telescope system consisting of a scan lens and a tube lens, the laser was focused onto the sample surface through an objective lens (NA = 0.5, Nikon, Corp.). The laser fluence was monitored by a photodiode. An ultrasonic transducer (HPM05/3, Precision Acoustics Ltd.) with a flat frequency spectrum from 200 kHz to 15 MHz was used to detect the PA signals. The signals were first amplified by a low-noise amplifier (LNA-650, RF BAY), and then transferred to a digital oscilloscope (DPO3034, Tektronix) and lock-in amplifier (OE2031, SYSU Scientific Instruments) to obtain the rise time and phase delay of PA signal, respectively. The function generator (AFG 1000, Tektronix) was used to simultaneously generate trigger signals T_1 (10 kHz), T_2 (10 kHz), and T_3 (1 MHz). The T_1 was used to trigger the pulsed laser; the T_2 and T_3 were used for triggering the oscilloscope and the lock-in amplifier, respectively. During the experiments, the laser fluence was controlled below the American National Standards Institute safety limit (20 mJ/cm^2) [46].

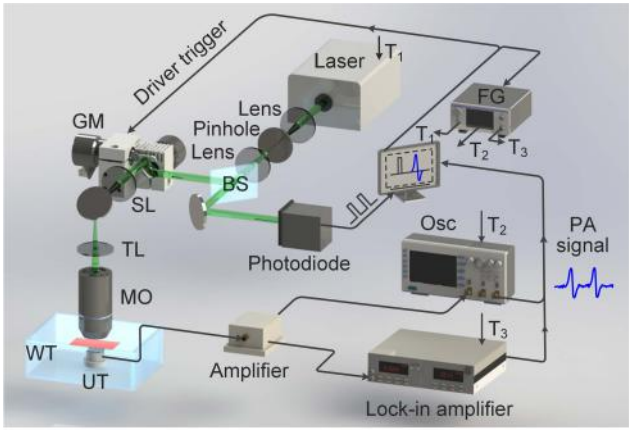

Fig. 2. Schematic setup of PAMR. BS, beam splitter; GM, galvanometer; SL, scan lens; TL, tube lens; MO, microscope objective; UT, ultrasonic transducer; WT, water tank; Osc, oscilloscope; FG, function generator. T_1, pulsed laser trigger; T_2, oscilloscope trigger; T_3, lock-in amplifier trigger.

A CCD camera (MD30, Mshot Co. Ltd, China) was installed to obtain optical picture of the sample.

D. Phantom and Cell Samples Preparation

In the validation experiment, an agar-gelatin based phantom was made with a mixture of agar powder, gelatin powder, and distilled water (agar: 3/4/5 g, gelatin: 3 g, water: 94 mL). The phantom contained three homogeneous fan-shaped inclusions with respective agar concentration of 30, 40, and 50 g/L (w/v). The inclusions with various agar concentrations were used to represent materials of different viscoelasticity values. Same-proportion (3%, v/v) India ink was respectively mixed in the three inclusions to provide optical absorption contrast. The three fan-shaped inclusions (thickness: 1.5 mm) were composed into a circular phantom with the diameter of ~24.0 mm and thickness of 1.5 mm. The target circular inclusion was surrounded by the background gel with 10 g/L (w/v) agar, 10 g/L (w/v) gelatin, and 0.5% (v/v) ink to form a $30 \times 30 \times 1.5$ mm^3 ($x \times y \times z$) square-shaped structure. Given the stiffness of the phantom could be affected by the temperature, all experiments were performed at constant room temperature of 25 °C.

In the cellular imaging experiment on myocyte and adipocyte, skin tissue slices crossing from dermis to subcutaneous tissue were collected from rat back, then immersed in 4% paraformaldehyde for 4 h and transferred to 70% ethanol. Specimens were embedded in paraffin wax blocks, and sectioned with 10 μm thickness on a microtome (RM2016, Leica, Germany). Tissue sections were dewaxed in xylene, rehydrated through decreasing concentrations of ethanol, and then washed. Finally, sections were placed on cover slide. The sections were examined by using a Nikon Eclipse microscope. All experimental animal procedures were carried out in conformity with a laboratory animal protocol approved by the South China Normal University.

In the rheology experiments on red blood cells (RBCs), the blood samples were collected from healthy adult donors and adult patients with iron deficiency anemia (IDA) in the Third Affiliated Hospital of Sun Yat-sen University. Informed consent was obtained from healthy donors and patients. The study was approved by the Institutional Review Board of the Third Affiliated Hospital of Sun Yat-sen University and South China Normal University. Experimental procedures were performed in accordance with the approved ethical guidelines. Patients were defined by the usual hematologic criteria. IDA was identified by a low mean cell volume (MCV) (<70 fL), low hemoglobin (HGB) (<110 g/L), elevated erythrocyte protoporphyrin (> 100 μg/dl RBC), and a low serum ferritin (<12 μg/L). Healthy control subjects were not anemic and have normal MCV, protoporphyrin, and serum ferritin values. After blood collection, RBCs were attached to the cover glass surface which was previously modified with poly-l-lysine (Sigma Aldrich, St Louis, MO, USA) solution. Poly-l-lysine assured the attachment of living erythrocytes on the glass surface due to the electrostatic interactions between negative charged RBCs and the positively charged poly-l-lysine surfaces. The following procedure of immobilization of cells onto glass was used. Firstly, the fresh blood sample were diluted in phosphate-buffered saline (PBS, Sigma) in the ratio of 1:1. Secondly, the blood samples were centrifuged at 2,000 rpm at 4 °C for 5 minutes to separate the RBCs from the whole blood samples, and then plasma and leukocyte layers were removed. Thirdly, the RBCs were washed twice with PBS buffer and collected from the bottom portion of the tube. Fourthly, the solution (two drops of blood solution) was placed on the glass substrate for 45 min. Afterwards, one drop of 0.5% glutaraldehyde solution was added for 1 min. Finally, such pretreated cells were washed with PBS in order to remove the unbounded cells and glutaraldehyde.

III. Results

A. Phantom Experiments

Proof-of-concept experiment was performed on homogeneous agar-gelatin based phantoms with respective agar concentration of 30, 40, and 50 g/L. Fig. 3(a) plots temporal PA signals of the phantoms with 30, 40, and 50 g/L agar concentration. In order to depress the noise, a lowpass filter (BLP-21.4+, Mini Circuits) and wavelet denoising have been performed on the raw PA signals. Inset in Fig. 3(a) is the photograph of the square-shaped phantom sample. The corresponding displacement according to (6) is shown in Fig. 3(b). As expected, the rise time decreases with increasing the agar concentration. The specific rise time and amplitude values of PA signals are depicted in Fig. 3(c). Eight independent measurements were recorded for each concentration phantom. Data-points and error bars indicate the mean measured value and the standard deviation (indicating repeatability) across the eight measurements. Fig. 3(c) shows independency of the rise time determination on the PA amplitude. The displacement data of 30 g/L agar phantom were fitted to the proposed model (Equation 4) to calculate the theoretical value of the rise time, as shown in Fig. 3(d). The difference in rise time estimated by the extraction procedure and that of the model fitting is about 4%, according to the least root mean square (LRMS) of the fit.

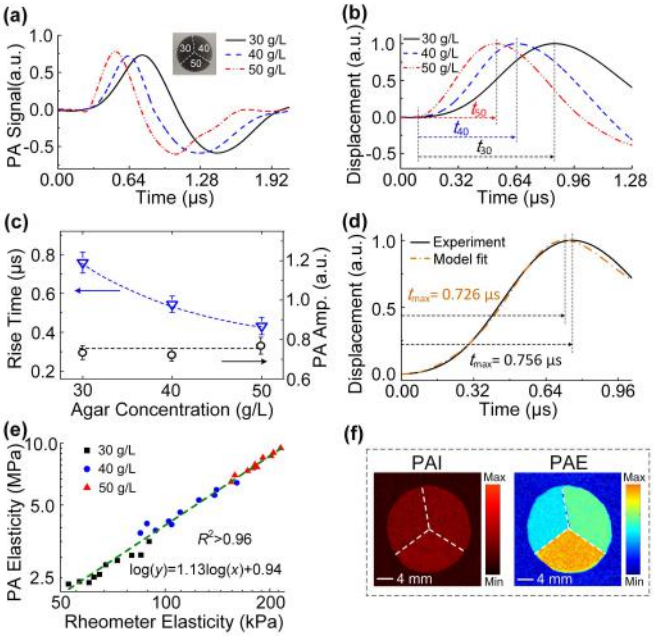

Fig. 3. Validation of the PA elasticity measurement method. (a) Temporal PA signals and (b) displacement of the phantoms with respective agar concentration of 30, 40, and 50 g/L. Inset in (a) is the photograph of the phantom sample. (c) Specific PA rise time and PA amplitude of the phantoms with different agar concentrations. (d) Displacement obtained by PA experimental measurement and by model fitting of the phantom with 30 g/L agar concentration. (e) Comparison between the elasticity obtained by the PA method and conventional rheometer. Dashed line, log-log linear fit. (f) The conventional PA amplitude image (PAI) and PA elastography (PAE). Error bars represent ± s. d.

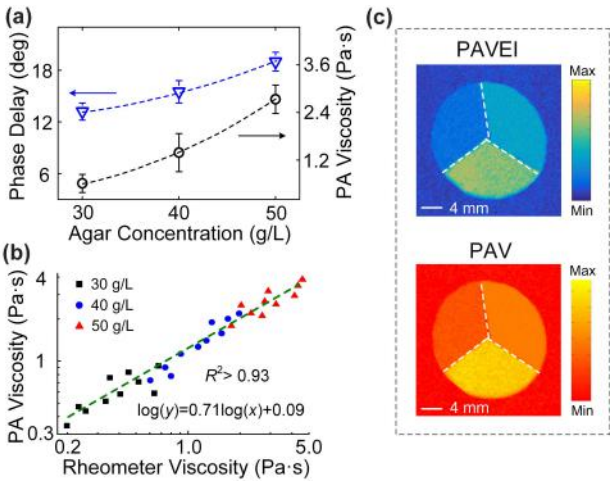

Fig. 4. Validation of the PA viscosity measurement method. (a) PA phase delay and corresponding viscosity of the phantoms with 30, 40, and 50 g/L agar concentration. (b) Comparison between the viscosity obtained by the PA method and conventional rheometer. Dashed line, log-log linear fit. (c) PA viscosity-elasticity ratio image (PAVEI) by phase delay measurement and the resulting PA viscography (PAV) from extracted elastic modulus and viscosity-elasticity ratio parameters. Error bars represent ± s. d.

The fitting results of 40 and 50 g/L agar phantoms are included in Supplementary Note 2. In the PA rheology measurement of the phantom, a 0.1 NA objective lens is used to enlarge scan range, and the waist radius R is estimated to be 38.5 μm by measuring the lateral resolution of the system (see Supplementary Note 3); ρ equals 1000 kg/m^3 based on *a priori*knowledge (e.g., values from the literature) [47]. PA elastic modulus is obtained according to (5). We compare the elasticity measured by the PA method and the conventional mechanical rheometer (AR-G2, TA Instruments, USA), as shown in Fig. 3(e). The mechanical testing result by rheometer is presented in Supplementary Note 4. Increasing the agar concentration leads to a significant increase in the elasticity, in agreement with the prior publications [29], [48]. This result indicates that the underlying biochemical and physical changes in the phantom affect both PA-derived longitudinal elastic modulus and rheometer-obtained shear elastic modulus in the same direction. A high correlation (R^2 >0.96) between the two moduli is obtained in curve fit to a log-log linear relationship. Such correlation has been consistently observed in biological tissues, as well as for polymers [49], [50]. It is worth noting that the elastic moduli values measured by those two methods are not matched, which attributes to the typically different frequencies for the two types of elastic moduli, because most biological materials exhibit viscoelastic properties characterized by frequency-dependent moduli [49]–[51]. More importantly, given the physical nature of the PA elastic modulus, i.e., longitudinal elastic modulus, which is distinct from the shear elastic modulus or Young's modulus, the observed large difference in their values is not surprising [49], [50], [52]. Fig. 3(f) shows the conventional PA amplitude image (PAI) and PA elastography (PAE). The images were obtained by a two-dimensional (2-D) stepper motor mechanically shifting the phantom sample (not shown). The stepper-motor scanning was used instead of the galvanometer scanning to enlarge scan range. The PAI presents no contrast in the amplitude image due to same optical absorption distribution. In contrast, PAE exhibits a significant difference in the elasticity. Biochemical composition or composition content rather than optical absorption contributes to the elasticity contrast. The results indicate the capability of the proposed method for elastic modulus determination.

Fig. 4(a) plots the phase delay between the PA response and laser excitation of the phantoms with 30, 40, and 50 g/L agar concentration. The phase delay was measured using the lock-in amplifier (see Supplementary Note 5). To avoid an extra distance-dependence phase delay deviation [34], the surface of the phantom was flattened by a cover glass. In addition, the transducer was fixed well to ensure same detection distance between the PA sources and the transducer. The corresponding PA viscosity is obtained from extracted elastic modulus and phase delay through (8) $\eta = E \tan\delta/\omega$, shown in Fig. 4(a). The viscosity exhibits a more significant variation than the phase delay with the agar concentration, which provides the possibility of PA viscography enabling a shaper contrast. To validate our method, we compare the PA-derived longitudinal viscosity with rheometer-obtained shear viscosity (see Supplementary Note 4) in Fig. 4(b). A log-log linear relationship (R^2 >0.93) between viscosity obtained by PA and rheometer is illustrated. The increase in viscosity with agar concentration due to a reduction in the ability to flow is also in good agreement with the previous studies [12], [53]. The minor difference

in the viscosity values measured with PA and rheometer methods is mainly due to the weak frequency dependence of the viscosity, which supports the attribution of the frequency (ω) to loss modulus ($\eta\omega$) [54], [55]. Fig. 4(c) provides the PA viscosity-elasticity ratio η/E image (PAVEI) based on the contrast of the phase delay through the relationship $\eta/E = \tan\delta/\omega$, and also provides the resulting PA viscography (PAV) from extracted elastic modulus and viscosity-elasticity ratio parameters. Both the PAVEI and PAV images can distinguish the agar phantoms with various mechanical properties. As expected, the PAV exhibits a sharper contrast than PAVEI, because the positive correlations between both the elasticity and viscosity parameters with the agar concentration weaken the influence of the concentration on the viscosity-elasticity ratio. The results explain the necessity of extracting both elastic modulus and viscosity respectively, instead of only viscosity-elasticity ratio, and also indicate the capability of the proposed method for viscosity determination.

B. Single-Cell Rheology on Adipocyte and Myocyte

To demonstrate image capability of PAMR on cells with different viscoelastic properties, the myocyte and adipocyte were tested. As illustrated in Fig. 5(a), the arrows indicate the adipocyte and myocyte in wide-field optical imaging. Fig. 5(b) plots time-domain PA signals of myocyte and adipocyte. Apparent difference exists in the rise time values between them. Myocyte exhibits a higher signal amplitude than adipocyte, which agrees well with the optical absorption-based contrast expectation. In contrast, the rise time of myocyte is lower than that of adipocyte. The result potentially indicates the amplitude and rise time characteristics of PA signal can provide different contrasts. Fig. 5(c) shows the phase delay of myocyte and adipocyte responses with respect to the laser stimulus. According to the measured rise time, phase delay, and amplitude information of PA response, the triple contrasts based on the elasticity, viscosity, and optical absorption are distinctly different in Fig. 5(d), where relative magnitudes of adipocyte are set to 1. The corresponding PA elastography (PAE), PA viscography (PAV), and conventional PA image (PAI) are presented in Fig. 5(e). The different properties distributions details of myocyte and adipocyte are clearly visible in these images. Elasticity and viscosity values are estimated according to (5) and (8), where the ρ and R is equal to 1000 kg/m^3 and 1.2 μm (see Supplementary Note 3), respectively. As expected, fiber-rich myocyte has a larger elasticity than lipid-rich adipocyte, because fiber is typically stiffer than the lipid. For PA viscography, the adipocyte shows a larger viscosity than myocyte due to the higher viscous dissipation of adipocyte than that of myocyte. Fig. 5(f) presents the distributions of the elastic modulus and viscosity along the lines (i) and (ii) in Fig. 5(e), with marked changes in the rheological parameters as a function of the cell sample position. An opposite distribution features of the elastic modulus and viscosity reveals that the two parameters are independent of each other. Further, the Young's moduli (see Supplementary Note 6) of the myocyte and adipocyte are measured with the atomic force microscopy (AFM) technique (Dimension Icon, Bruker, Germany). The sample preparation is same for PA and AFM measurements. Fig. 5(g) shows a high correlation ($R^2 > 0.94$) in log-log linear relationship between the apparent PA longitudinal elastic modulus and AFM-obtained Young's modulus. As emphasized previously, the observed large difference within the elasticity metrics obtained by both techniques can be ascribed to the different physical natures of the longitudinal and Young's moduli as well as to the frequency dependence of the elasticity [49]–[52]. The results indicate that PAMR has the ability to distinguish diverse cell types with various rheological properties.

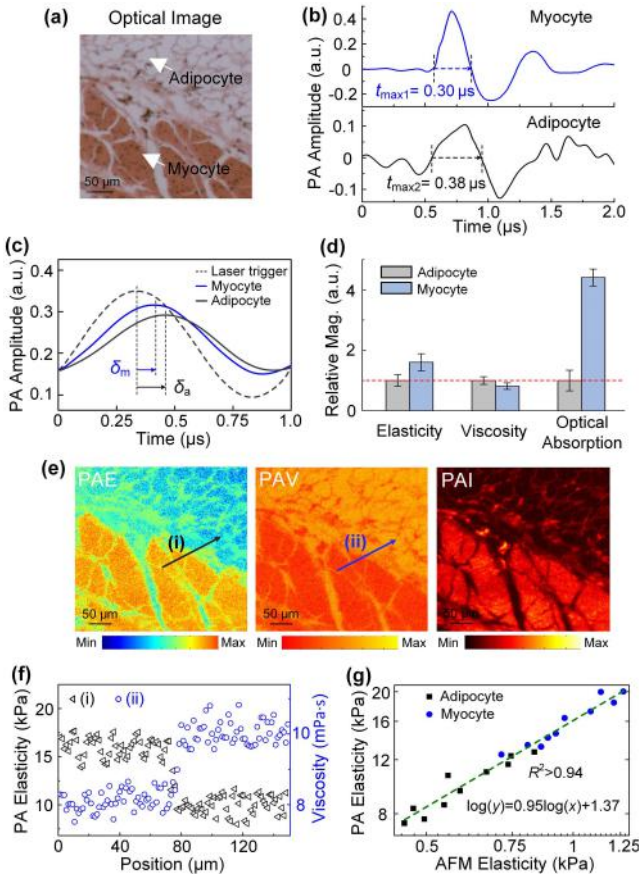

Fig. 5. Rheology on adipocyte and myocyte. (a) Wide-field optical image of sample. (b) Time-domain PA signals of myocyte and adipocyte. (c) Phase delays of PA responses with respect to the laser trigger for myocyte and adipocyte. (d) The relative magnitude (mag.) of elasticity, viscosity, and optical absorption parameters of myocyte and adipocyte. (e) The representative PA elastography (PAE), PA viscography (PAV), and conventional PA image (PAI). (f) Elasticity and viscosity distributions along the lines (i) and (ii) in (e). (g) Comparison of elastic modulus measured using PA method and AFM. Each data point is the average of 5 measurements on 10 different adipocytes and myocytes.

C. Single-Cell Rheology on RBCs from Iron Deficiency Anemia

Aspects of mechanical deformability and biorheology of the red blood cell (RBC) are known to play a pivotal role in influencing organ function as well as states of overall health and disease, such as sickle cell anemia, iron deficiency anemia, and hereditary spherocytosis [56], [57]. The ability of our technique to detect rheological variations was also

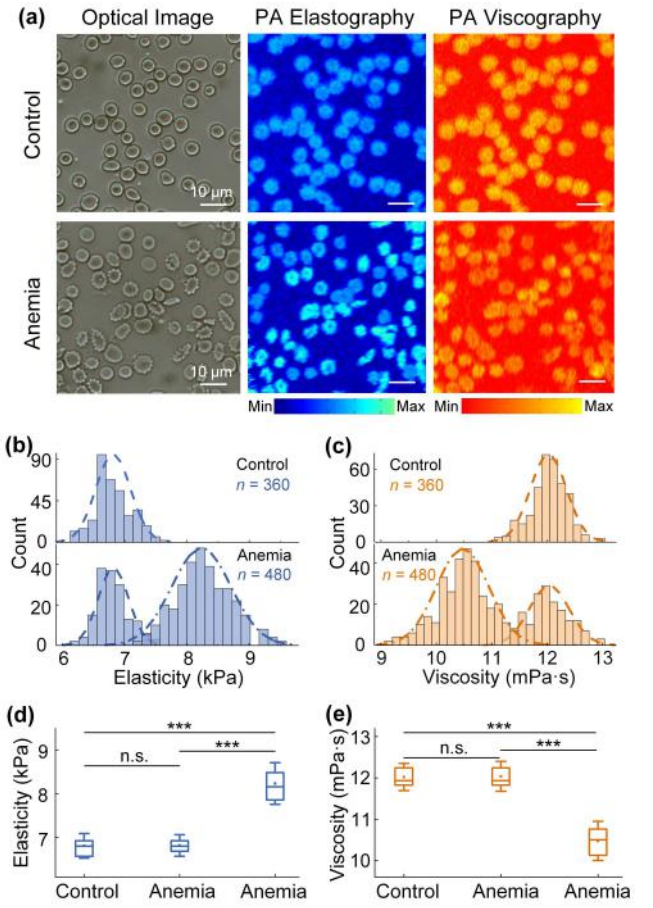

Fig. 6. Rheology of normal red blood cells (RBCs) and iron deficiency anemia (IDA) RBCs. (a) Wide-field optical image (first column), PA elastography (second column), and PA viscography (third column) of RBCs from control and anemia subjects. (b) and (c) Histograms of apparent elastic modulus and apparent viscosity for RBCs from normal and IDA subjects. The dashed lines are the Gaussian fits, and the Gaussian peak represents the average values of apparent elasticity and viscosity. (d) and (e) Statistical analysis of apparent elastic modulus and apparent viscosity for RBCs comparing control subject ($n = 360$) and anemia subject ($n = 480$). Data in each group is 6–8 sampling points on 60 different cells. Error bars represent standard error of the mean; n.s., not significant, $***$ $p < 0.001$, unpaired two-tailed t-test. Scale bars, 10 μm.

tested by comparing the PA data acquired in the RBCs from healthy adult donors and adult patients with iron deficiency anemia (IDA). Fig. 6(a) shows wide-field optical images (first column) of RBCs from control subject and anemia patient. RBCs of control subject show uniform sizes and regular shapes. In contrast, uneven sizes and irregular profiles such as oval and elongated shapes are observed in anemia subject. For PA elastography (second column) in Fig. 6(a), several RBCs of anemia subject show an increase in the apparent elastic modulus relative to the control subject, which can be attributed in part to lipid peroxidation. Increased membrane stiffness reduces membrane deformability, favoring impaired red cell survival in iron deficiency. Elasticity increase in iron-deficient RBC agrees well with the literatures previously reported [58], [59]. In addition, the other RBCs in anemia subject show no significant difference in the elastic modulus with respect to control subject. This perhaps indicates two populations of RBCs in the IDA samples—normal and pathological ones. Depending on the position we focus on, the elastic modulus of the single cell exhibits a fluctuation: the cell center gives a smaller elasticity than the cell edge [60]. Further, PA viscosity (third column) of RBCs from control and IDA subjects are then mapped in Fig. 6(a). Contrary to elasticity variation, lower viscosity is observed in iron-deficient RBCs due to peroxidation of the lipid and cross-linking of erythrocyte proteins [57].

Fig. 6(b) shows the elasticity histograms for RBCs in control and anemia subjects. The bin size of elasticity histogram is 145 Pa, and the average value of elastic modulus is obtained by the Gaussian fit. In anemia subject, the two peaks in histogram are observed with an apparent elastic modulus $E = 8.23 \pm 0.47$ kPa and $E = 6.82 \pm 0.25$ kPa respectively, which are significantly increased and slightly reduced compared to the normal RBCs in control subject with an apparent elastic modulus $E = 6.81 \pm 0.28$ kPa. This demonstrates in the IDA sample the presence of two RBC populations—normal and pathological ones. Fig. 6(c) shows RBCs viscosity histograms for control and anemia subjects, and the bin size of histogram is 142 μPa·s. For RBCs in anemia subject, we also found the two peaks of apparent viscosities $\eta = 10.47 \pm 0.46$ mPa·s and $\eta = 12.04 \pm 0.36$ mPa·s respectively, which reveals a marked decrease and no obvious difference relative to the control RBCs with a viscosity $\eta = 12.02 \pm 0.33$ mPa·s. Figs. 6(d) and 6(e) exhibit the statistical analyses of two rheological parameters over normal and anemia subjects each consisting of 60 different single RBCs with 6-8 sampling points. Estimations of the apparent elasticity and viscosity yield statistically significant differences for the normal and iron-deficient RBCs. Iron-deficient RBCs present an increase ($\sim$21%) in the elastic modulus and a decrease ($\sim$13%) in the viscosity compared to the normal ones. For normal RBCs in control and IDA samples, no significant difference is observed on both elasticity and viscosity. The results demonstrate the potential application of PAMR technique in the identification of hematologic diseases.

IV. Discussion

The preliminary results of this study are promising, indicating the feasibility of the proposed method for mapping rheological properties of tissues and cells. Compared with existing elasticity measurement techniques, PAMR does not require extrinsic mechanical loading, i.e., a contactless manner. This feature of being non-contact makes it particularly well suited to many applications, such as cell, ophthalmology, endoscopy, and wounds or burns. In addition, the proposed technique operates in label-free conditions and in a non-invasive manner, favoring *in vivo* cell functionality analysis and the future biomedical applications. PAMR technique realizes simultaneous measurement of elasticity and viscosity, instead of being limited to elasticity assessment as most of existing mechanical properties measurement methods. Ignoring viscosity would lose important information about tissue physiological state and diminish the diagnostic accuracy. For instance, clinical ultrasound shear wave elastography study shows a significant false-positive rate in early cirrhosis diagnosis when the liver

is inflamed, owing to the lack of assessment of the hepatitis-induced viscosity changes [61], [62]. PAMR is easily implemented on existing PA imaging system, which will enable multi-contrast imaging modalities based on PA technique to provide the morphological, mechanical, and functional information of cells and tissues for disease diagnosis and treatment evaluation. It is also readily miniaturized, opening the possibility to provide small footprint probes, for example, in endoscopic and needle formats. In the future, the applicability of the PAMR technique can be extended to tumor cell functionality analysis. For example, tumor cells show the overall reduction in elasticity and viscosity involved in malignant transformation. Because this can enhance cellular deformability, favoring *in vivo* dissemination and metastasis [52].

For most biological materials, the elastic modulus is usually frequency dependent. Slower relaxation processes have little time to respond to fast excitation and, thus the modulus tends to increase with the frequency [50]. Even so, the absolute measurement of elastic modulus can be conducted with PA method. For PA response, its typical time scale is on the order of microsecond, which corresponds to the characteristic frequency of megahertz. For example, an ultrasonic transducer with MHz bandwidth is usually used to detect the PA wave. In the PA rheology experiment, laser excitation frequency (10 kHz) lower than material's characteristic frequency (MHz) was used to obtain the real response of material to the excitation. Thus, in this case, the laser excitation frequency would not affect the magnitude of the PA elastic modulus.

However, further efforts are made to improve the technique and make it more acceptable to the biomedical application. To compute the elastic modulus, sample density is assumed to be a constant value. This is an approximation, as density is not uniform throughout cells and likely changes under different osmotic conditions; however, the changes in density did not substantially affect the elastic modulus estimation ($\sim$1% error) [24], [49]. Constant value for density is the common assumption for most elasticity measurement technique, such as ultrasound elastography, AFM, and optical coherence elastography [11], [22], [24].

Our proposed model of medium response used to estimate elastic modulus has been simplified by necessity to allow for an analytic solution. The model focuses on the shallow surface excitation of sample. A challenge is that sample geometry and optical absorption properties would affect the PA signal profile. In this work, the optical illumination has been limited to a point spot, i.e., a microscopy mode, to effectively reduce the influence of the sample geometry and optical absorption distribution due to the tight optical focusing on sample superficial region. In future studies, a dedicated optic-acoustic confocal probe with large numerical aperture is required to minimize the influence of these factors by tightly focusing both light and ultrasound. In addition, the higher complexity and integrality of models that are more faithful to complex biology properties will invariably necessitate the use of numerical computation to extract the mechanical parameters more accurately. Fundamentally, a promising avenue to address challenges lies in considering a bulk absorption model based on the Lambert-Beer law to decouple the influence of the sample geometry and optical absorption properties. The bulk absorption model is also expected to differentiate the PA signals from different depths to obtain viscoelasticity tomography and then three-dimensional rheological properties mappings.

The bandwidth of the ultrasound transducer could affect the PA signal waveform. However, we would like to emphasize that the bandwidth only has an impact on the absolute magnitude but not on the relative differences of the PA rise time from different kinds of samples. Since different initial PA signals from different samples will experience the same frequency response of the transducer, generating still different PA signal profiles and rise times for elasticity measurement. It also would not affect the observed statistical trends, because statistical analysis is based on linear mixed models comparing replicates of one group of samples to another group. Moreover, the influence of the transducer's bandwidth on the absolute value of the elastic modulus can be eliminated by introducing a calibration constant, since the actual values always depend on the measurement system [20], [49]. The calibration factor can be experimentally determined by using a standardized elastic solid with the known elastic modulus value. While the low bandwidth of the transducer will make measured rise time longer, it also results in smaller calibration factor for the standardized elastic solid. Thus, in the PA measurement, overestimation of the measured rise time and smaller calibration factor would not affect the determination of calibrated PA elastic modulus. To reduce the influence of the limited bandwidth of ultrasound transducer as much as possible, a wide-band polyvinylidene fluoride (PVDF) transducer with a flat frequency response from 200 kHz to 15 MHz has been used in PA rheology experiment. In the future, a more broadband transducer or all-optical technique will be utilized to minimize the influence. All-optical technique to perform the PAMR is not only capable of detecting signals with ultrabroad bandwidth, but also of facilitating technical implementation due to coupling-free fashion [63].

The precision of rise time estimation depends largely on the bandwidth of the ultrasound transducer and noise level. With the transducer bandwidth of $\sim$15 MHz, the time resolution of 4 ns, and the signal-to-noise ratio (SNR) of 10 dB, our instrument is able to detect a $\sim$3.2% change in the elastic modulus (see Supplementary Note 7). The precision can be further improved by an ultrasound transducer with broader bandwidth or an all-optical technique and by an enhancement in SNR. The way to enhance SNR is to utilize low-noise amplifier with higher gain and more data averaging or other technique, such as coherent correlation. Therefore, with an advanced theoretical model, an improved reconstruction algorithm, and a dedicated system design and optimization, PAMR can provide a more robust method for elastic modulus and viscosity estimations with higher accuracy and reliability.

V. Conclusion

In conclusion, we developed a novel PA microrheology to extract cellular elasticity and viscosity correlated with their biochemical composition in a contactless condition, i.e., without indentation. The method utilizes time and phase

characteristics of PA response for biomechanical properties investigation, which potentially opens new perspectives of conventional optical-absorption-based PA amplitude imaging. Thanks to its noninvasive image manner and relative simplicity, PAMR can become a unique tool for interrogating biomechanical properties in future biomedical applications.

Acknowledgment

The authors thank Dr. Y. Shi for her valuable advices to this article. They also thank the Third Affiliated Hospital of Sun Yat-sen University for providing blood samples.

References

[1] P. A. Pullarkat, P. A. Fernández, and A. Ott, "Rheological properties of the Eukaryotic cell cytoskeleton," *Phys. Rep.*, vol. 449, nos. 1–3, pp. 29–53, Sep. 2007.

[2] M. P. Stewart, J. Helenius, Y. Toyoda, S. P. Ramanathan, D. J. Müller, and A. A. Hyman, "Hydrostatic pressure and the actomyosin cortex drive mitotic cell rounding," *Nature*, vol. 469, no. 7329, pp. 226–230, Jan. 2011.

[3] F. Lautenschläger, S. Paschke, S. Schinkinger, A. Bruel, M. Beil, and J. Guck, "The regulatory role of cell mechanics for migration of differentiating myeloid cells," *Proc. Nat. Acad. Sci. USA*, vol. 106, no. 37, pp. 15696–15701, Sep. 2009.

[4] S. E. Cross, Y. S. Jin, J. Rao, and J. K. Gimzewski, "Nanomechanical analysis of cells from cancer patients," *Nature Nanotechnol.*, vol. 2, no. 12, pp. 780–783, Dec. 2007.

[5] D. Ingber, "Mechanobiology and diseases of mechanotransduction," *Ann. Med.*, vol. 35, no. 8, pp. 564–577, Jan. 2003.

[6] M. A. Haidekker and E. A. Theodorakis, "Molecular rotors-fluorescent biosensors for viscosity and flow," *Organic Biomol. Chem.*, vol. 5, no. 11, pp. 1669–1678, Jul. 2007.

[7] S. J. Singer and G. L. Nicolson, "The fluid mosaic model of the structure of cell membranes," *Science*, vol. 175, pp. 720–731, Feb. 1972.

[8] M. Shinitzky, *Physiology of Membrane Fluidity*. Boca Raton, FL, USA: CRC Press, 1984.

[9] K. N. Dahl, A. J. S. Ribeiro, and J. Lammerding, "Nuclear shape, mechanics, and mechanotransduction," *Circulat. Res.*, vol. 102, no. 11, pp. 1307–1318, Jul. 2008.

[10] J. D. Pajerowski, K. N. Dahl, F. L. Zhong, P. J. Sammak, and D. E. Discher, "Physical plasticity of the nucleus in stem cell differentiation," *Proc. Nat. Acad. Sci. USA*, vol. 104, no. 40, pp. 15619–15624, Oct. 2007.

[11] S. Chen, M. Fatemi, and J. F. Greenleaf, "Quantifying elasticity and viscosity from measurement of shear wave speed dispersion," *J. Acoust. Soc. Amer.*, vol. 115, no. 6, pp. 2781–2785, Jun. 2004.

[12] C.-C. Shih *et al.*, "Quantitative assessment of thin-layer tissue viscoelastic properties using ultrasonic micro-elastography with Lamb wave model," *IEEE Trans. Med. Imag.*, vol. 37, no. 8, pp. 1887–1898, Aug. 2018.

[13] P. Kijanka and M. W. Urban, "Local phase velocity based imaging: A new technique used for ultrasound shear wave elastography," *IEEE Trans. Med. Imag.*, vol. 38, no. 4, pp. 894–908, Apr. 2019.

[14] P. G. Mongrain *et al.*, "Ultrafast imaging of cell elasticity with optical microelastography," *Proc. Nat. Acad. Sci. USA*, vol. 115, no. 5, pp. 1–6, Jan. 2018.

[15] J. Zhu *et al.*, "Imaging and characterizing shear wave and shear modulus under orthogonal acoustic radiation force excitation using OCT Doppler variance method," *Opt. Lett.*, vol. 40, no. 9, pp. 2099–2102, May 2015.

[16] C. Bustamante, Z. Bryant, and S. B. Smith, "Ten years of tension: Single-molecule DNA mechanics," *Nature*, vol. 421, pp. 423–427, Feb. 2003.

[17] D. Chen *et al.*, "Two-bubble acoustic tweezing cytometry for biomechanical probing and stimulation of cells," *Biophys. J.*, vol. 108, no. 1, pp. 32–42, Jan. 2015.

[18] S. B. Smith, L. Finzi, and C. Bustamante, "Direct mechanical measurements of the elasticity of single DNA-molecules by using magnetic beads," *Science*, vol. 258, no. 5085, pp. 1122–1126, Nov. 1992.

[19] G. S. Worthen, B. Schwab, E. L. Elson, and G. P. Downey, "Mechanics of stimulated neutrophils: Cell stiffening induces retention in capillaries," *Science*, vol. 245, no. 4914, pp. 183–186, Jul. 1989.

[20] B. Fregin *et al.*, "High-throughput single-cell rheology in complex samples by dynamic real-time deformability cytometry," *Nature Commun.*, vol. 10, no. 1, p. 415, Jan. 2019.

[21] H. Engelhardt, H. Gaub, and E. Sackmann, "Viscoelastic properties of erythrocyte membranes in high-frequency electric fields," *Nature*, vol. 307, no. 5949, pp. 378–380, Jan. 1984.

[22] S. Lee *et al.*, "Super-resolution visible photoactivated atomic force microscopy," *Light Sci. Appl.*, vol. 6, no. 11, May 2017, Art. no. e17080.

[23] G. Scarcelli and S. H. Yun, "Confocal Brillouin microscopy for three-dimensional mechanical imaging," *Nature Photon.*, vol. 2, no. 1, pp. 39–43, Dec. 2007.

[24] B. F. Kennedy, P. Wijesinghe, and D. D. Sampson, "The emergence of optical elastography in biomedicine," *Nature Photon.*, vol. 11, no. 4, pp. 215–221, Apr. 2017.

[25] L. V. Wang and S. Hu, "Photoacoustic tomography: *In vivo* imaging from organelles to organs," *Science*, vol. 335, pp. 1458–1462, Mar. 2012.

[26] P. Beard, "Biomedical photoacoustic imaging," *Interface Focus*, vol. 1, no. 4, pp. 602–631, Aug. 2011.

[27] J. Xia and L. V. Wang, "Small-animal whole-body photoacoustic tomography: A review," *IEEE Trans. Biomed. Eng.*, vol. 61, no. 5, pp. 1380–1389, May 2014.

[28] P. Hai, J. Yao, G. Li, C. Li, and L. V. Wang, "Photoacoustic elastography," *Opt. Lett.*, vol. 41, no. 4, pp. 4725–4728, Feb. 2016.

[29] M. S. Singh and H. Jiang, "Elastic property attributes to photoacoustic signals: An experimental phantom study," *Opt. Lett.*, vol. 39, no. 13, pp. 3970–3973, Jul. 2014.

[30] Y. Liu and Z. Yuan, "Multi-spectral photoacoustic elasticity tomography," *Biomed. Opt. Express*, vol. 7, no. 9, pp. 3323–3334, Sep. 2016.

[31] G. Gao, S. Yang, and D. Xing, "Viscoelasticity imaging of biological tissues with phase-resolved photoacoustic measurement," *Opt. Lett.*, vol. 36, no. 17, pp. 3341–3343, Sep. 2011.

[32] Y. Zhao, S. Yang, C. Chen, and D. Xing, "Simultaneous optical absorption and viscoelasticity imaging based on photoacoustic lock-in measurement," *Opt. Lett.*, vol. 39, no. 9, pp. 2565–2568, May 2014.

[33] D. Jin, F. Yang, Z. Chen, S. Yang, and D. Xing, "Biomechanical and morphological multi-parameter photoacoustic endoscope for identification of early esophageal disease," *Appl. Phys. Lett.*, vol. 111, no. 10, Sep. 2017, Art. no. 103703.

[34] C. Chen, Y. Zhao, S. Yang, and D. Xing, "Integrated mechanical and structural features for photoacoustic characterization of atherosclerosis using a quasi-continuous laser," *Opt. Express*, vol. 23, no. 13, pp. 17309–17315, Jun. 2015.

[35] Y. Zhao, C. Chen, S. Yang, and D. Xing, "Mechanical evaluation of lipid accumulation in atherosclerotic tissues by photoacoustic viscoelasticity imaging," *Opt. Lett.*, vol. 41, no. 19, pp. 4522–4525, Oct. 2016.

[36] W. M. Lai, D. Rubin, and E. Krempl, *Introduction to Continuum Mechanics*. Oxford, U.K.: Butterworth-Heinemann, 2010.

[37] H. Zhu, "Elastic wavefield separation based on the Helmholtz decomposition," *Geophysics*, vol. 82, no. 2, pp. S173–S183, Feb. 2017.

[38] V. E. Gusev and A. A. Karabutov, *Laser Optoacoustics*. New York, NY, USA: American Institute of Physics, 1993.

[39] C. Lou, S. Yang, Z. Ji, Q. Chen, and D. Xing, "Ultrashort microwave-induced thermoacoustic imaging: A breakthrough in excitation efficiency and spatial resolution," *Phys. Rev. Lett.*, vol. 109, no. 21, Nov. 2012, Art. no. 218101.

[40] R. B. Hetnarski, *Thermal Stresses*. Amsterdam, The Netherlands: Elsevier, 1996.

[41] A. P. Sarvazyan, O. V. Rudenko, S. D. Swanson, J. B. Fowlkes, and S. Y. Emelianov, "Shear wave elasticity imaging: A new ultrasonic technology of medical diagnostics," *Ultrasound Med. Biol.*, vol. 24, no. 9, pp. 1419–1435, Dec. 1998.

[42] I. G. Calasso, W. Craig, and G. J. Diebold, "Photoacoustic point source," *Phys. Rev. Lett.*, vol. 86, no. 16, pp. 3550–3553, May 2001.

[43] Y.-C. Fung, *Biomechanics: Mechanical Properties of Living Tissues*. New York, NY, USA: Springer, 2013.

[44] P. H. Wu *et al.*, "A comparison of methods to assess cell mechanical properties," *Nature Methods*, vol. 15, no. 7, pp. 491–498, Jul. 2018.

[45] T. G. Mason and D. A. Weitz, "Optical measurements of frequency-dependent linear viscoelastic moduli of complex fluids," *Phys. Rev. Lett.*, vol. 74, no. 7, pp. 1250–1253, Feb. 1995.

[46] *American National Standard for Safe Use of Lasers*. Orlando, FL, USA: Laser Institute of America, 2014.

[47] F. A. Duck, *Physical Properties of Tissues: A Comprehensive Reference Book*. London, U.K.: Academic, 1990.

[48] T. J. Hall, M. Bilgen, M. F. Insana, and T. A. Krouskop, "Phantom materials for elastography," *IEEE Trans. Ultrason., Ferroelectr., Freq. Control*, vol. 44, no. 6, pp. 1355–1365, Jun. 1997.

[49] G. Scarcelli *et al.*, "Noncontact three-dimensional mapping of intracellular hydromechanical properties by Brillouin microscopy," *Nature Methods*, vol. 12, no. 12, pp. 1132–1134, Oct. 2015.
[50] G. Scarcelli, P. Kim, and S. H. Yun, "In vivo measurement of age-related stiffening in the crystalline lens by Brillouin optical microscopy," *Biophys. J.*, vol. 101, no. 6, pp. 1539–1545, Sep. 2011.
[51] M. R. K. Mofrad and R. D. Kamm, *Cytoskeletal Mechanics: Models and Measurements in Cell Mechanics*. New York, NY, USA: Cambridge Univ. Press, 2006.
[52] S. Mattana *et al.*, "Non-contact mechanical and chemical analysis of single living cells by microspectroscopic techniques," *Light Sci. Appl.*, vol. 7, no. 2, 2018, Art. no. 17139.
[53] N. Gavara and R. S. Chadwick, "Noncontact microrheology at acoustic frequencies using frequency-modulated atomic force microscopy," *Nature Methods*, vol. 7, no. 8, pp. 650–654, Aug. 2010.
[54] I. Sack, B. Beierbach, U. Hamhaber, D. Klatt, and J. Braun, "Non-invasive measurement of brain viscoelasticity using magnetic resonance elastography," *NMR Biomed.*, vol. 21, no. 3, pp. 265–271, Apr. 2008.
[55] Y. Zhu *et al.*, "The role of viscosity estimation for oil-in-gelatin phantom in shear wave based ultrasound elastography," *Ultrasound Med. Biol.*, vol. 41, no. 2, pp. 601–609, Feb. 2015.
[56] S. Suresh, "Mechanical response of human red blood cells in health and disease: Some structure-property-function relationships," *J. Mater. Res.*, vol. 21, no. 8, pp. 1871–1877, Aug. 2006.
[57] Y. Chen *et al.*, "Effect of N-ethylmaleimide, chymotrypsin, and H_2O_2 on the viscoelasticity of human erythrocytes: Experimental measurement and theoretical analysis," *J. Biophoton.*, vol. 7, no. 8, pp. 647–655, Aug. 2014.
[58] I. Dulińska *et al.*, "Stiffness of normal and pathological erythrocytes studied by means of atomic force microscopy," *J. Biochem. Biophys. Methods*, vol. 66, pp. 1–11, Apr. 2006.
[59] R. Yip, N. Mohandas, M. R. Clark, S. Jain, S. B. Shohet, and P. R. Dallman, "Red cell membrane stiffness in iron deficiency," *Blood*, vol. 62, no. 1, pp. 99–106, Aug. 1983.
[60] Z. Meng, S. C. B. Lopez, K. E. Meissner, and V. V. Yakovlev, "Subcellular measurements of mechanical and chemical properties using dual Raman-Brillouin microspectroscopy," *J. Biophoton.*, vol. 9, no. 3, pp. 201–207, Nov. 2015.
[61] X. Chen *et al.*, "Quantification of liver viscoelasticity with acoustic radiation force: A study of hepatic fibrosis in a rat model," *Ultrasound Med. Biol.*, vol. 39, no. 11, pp. 2091–2102, Nov. 2013.
[62] G. Ferraioli, C. Tinelli, B. D. Bello, M. Zicchetti, G. Filice, and C. Filice, "Accuracy of real-time shear wave elastography for assessing liver fibrosis in chronic hepatitis C: A pilot study," *Hepatology*, vol. 56, no. 6, pp. 2125–2133, Dec. 2012.
[63] Z. Chen, S. Yang, Y. Wang, and D. Xing, "All-optically integrated photo-acoustic microscopy and optical coherence tomography based on a single Michelson detector," *Opt. Lett.*, vol. 40, no. 12, pp. 2838–2841, Jun. 2015.